Journal Name

ARTICLE TYPE

Cite this: DOI: 00.0000/xxxxxxxxxx

Interplay between synthetic conditions and micromorphology in poly(3,4-ethylenedioxythiophene) (PEDOT) for thermoelectric applications: An atomistic investigation†

A. Cappai,[a] A. Antidormi,[a] A. Bosin,[a] D. Galliani,[b‡] D. Narducci,[b‡] and C. Melis[a]

Received Date
Accepted Date

DOI: 00.0000/xxxxxxxxxx

Micromorphology of conjugated polymers are expected to play a crucial role on their thermoelectric performances by affecting both heat and charge transport. In this perspective, the details of the polymerization mechanism acquires a fundamental relevance, providing the link between the basic chemical reaction paths and the resulting molecular structure and arrangement. For PEDOT, it is still a matter of debate the role played by the Brønsted bases (proton scavengers) and their impact on the distribution of polymer chain lengths. In the present work we have systematically analyzed several reaction paths leading to PEDOT polymerization. By means of atomistic simulations we identified the thermodynamically preferred reaction path, proving that tosylate anions rule proton scavenging. PEDOT chain length was computed to be $\sim$ 12-13 monomeric units. We could also demonstrate how the proton scavengers set at once the chain lengths and the sample crystallinity. Furthermore, we found that tosylate gives rise to a sharper multimodal distribution of chain length, a feature that supports hypotheses advanced about the occurrence of a percolative transport regime mediated by tie chains bridging paracrystalline regions.

1 Introduction

Among conjugated polymers, poly(3,4-ethylenedioxythiophene) (PEDOT) displays a valuable combination of high electrical conductivity and intrinsically low thermal conductivity[1,2]. This feature, along with its high temperature stability[3], has attracted the interest of scientists in view of its use as a thermoelectric material. Relatively large values of the thermoelectric figure of merit have been reported for differently synthesized PEDOT samples[4]. Still, such values are too low compared to state-of-the-art inorganic thermoelectric materials, which often display thermoelectric figures of merit larger than one[5]. As a result, great effort has been devoted to improve PEDOT performance, mainly by increasing its power factor. It is interesting to note that, despite PEDOT allegedly consists of relatively short chains, its electrical conductivity is among the largest reported in conjugated polymers[6]. This has led to conjecture charge carrier mechanisms qualitatively different from those reported for other conjugated polymers[7]. This counterintuitive evidence motivates a deeper investigation of the interplay between PEDOT chain length distribution, microstructure and the transport mechanism. In this perspective, the polymerization mechanism acquires a fundamental relevance, as it links PEDOT chain length and arrangement to the underlying chemical reaction path. Specifically, the role of all chemical species involved in the polymerization needs to be more clearly established, along with their effect on the distribution of polymer chain lengths and on PEDOT crystallinity[8].

Aim of this paper is to report about a computational analysis of the microstructure of PEDOT. Since the reaction path leading to the polymerization impacts the chain length distribution and, consequently, the polymer microstructure, the procedure we have followed numerically replicates the formation of the polymer and its concurrent arrangement (packing). To this purpose, we set up a novel computational protocol based on a hierarchical combination of two different atomistic simulation techniques, i.e. first-principles density functional theory (DFT) and classical molecular dynamics (MD). By means of DFT calculations we compared with quantum mechanical accuracy each candidate chemical species as proton scavenger. Next, based on DFT results we simulated the polymerization process, considering all candidate Brønsted

[a] *Department of Physics, Univ. of Cagliari, Cittadella Universitaria, 09042 Monserrato, Italy*

[b] *Department of Material Science, Univ. of Milano-Bicocca, 20125 Milano, Italy*

† Electronic Supplementary Information (ESI) available: [details of any supplementary information available should be included here]. See DOI: 00.0000/00000000.

‡ Additional footnotes to the title and authors can be included *e.g.* 'Present address:' or 'These authors contributed equally to this work' as above using the symbols: ‡, §, and ¶. Please place the appropriate symbol next to the author's name and include a `\footnotetext` entry in the the correct place in the list.

bases. This led to realistic PEDOT samples, wherein PEDOT micromorphology (chain length distribution and crystallinity) was investigated.

It will be shown that proton scavenging, chain length distribution, and polymer crystallinity are strictly intertwined issues. The efficiency of the proton scavenger in capturing protons will be shown to be crucial to trigger the polymerization reaction, also in agreement with previous experimental studies[9,10]. However, experiments may hardly identify the proton scavenger univocally. Instead, computational analyses may more easily disentangle the role of bases in the polymerization process, also confirming experimental claims indirectly showing the key role played by the proton scavenger to set PEDOT chain lengths, varying from 7 up to 20 monomeric units depending on reaction conditions[11–13]. We anticipate that proton scavengers are found to strongly impact PEDOT molecular weight yielding chain lengths from ∼4 up to ∼20 monomeric units. The corresponding sample micromorphologies are also affected, with crystallinity fractions ranging from ∼ 1% up to ∼ 50%.

2 Method

2.1 DFT calculations

For each polymerization reaction

$$HX_{n-1}H^+ + HXH^+ + B + B' \rightleftharpoons HX_nH + BH^+ + B'H^+$$

(where HXH stands for the EDOT monomer and B and B' for the proton scavengers), we estimate the Gibbs free energy of reaction $\Delta G(n)$ (where n is the number of monomers composing the oligomer) using a different combination of molecules as proton scavengers. All the calculations are performed both in solution and in vacuo using the Gaussian16 suite of programs[14]. In order to calculate gas phase Gibbs free energies ΔG^0 all the geometries were first optimized at the B3LYP/6-311G(d,p) level and a vibrational frequencies calculation was then performed at the same theory level. The same procedure was employed to estimate the Gibbs free energies in solution $\Delta G_{\rm sol}$ by using the SMD implicit solvent model[15].

Specifically, the Gibbs free energy of reaction is calculated as:

$$\Delta G = \Delta G^0 + \Delta G^{0\to *} + \Delta G_{\rm sol} \quad (1)$$

where

- ΔG^0 is the gas-phase Gibbs free energy of reaction;
- $\Delta G^{0\to *}$ is the Gibbs free energy of transfer from the gas phase to the solution[16]

$$\Delta G^{0\to *} = \Delta nRT \ln\left(\frac{RT}{pV^*}\right) \quad (2)$$

  where Δn is the difference between the sum of moles of products and the sum of moles of reactants, p is the gas phase pressure (1 atm, in the present case), $1/V^*$ is the solute concentration (assumed to be 1 mol/L), T the absolute temperature and R is the gas constant.
- $\Delta G_{\rm sol}$ is the solvatation Gibbs free energy accounting for solute-solvent interactions for each reactant and product.

Table 1 Comparison between the computed dissociation enthalpy $\Delta H^{\rm theo}_{298}$ and entropy $\Delta S^{\rm theo}_{298}$ with the corresponding experimental values. Enthalpies are expressed in kcal/mol while entropies are in cal/mol/K.

Species	$\Delta H^{\rm theo}_{298}$	$\Delta H^{\rm exp}_{298}$	$\Delta S^{\rm theo}_{298}$	$\Delta S^{\rm exp}_{298}$
HBr	324.91	323.5	47	47.425
HCl	329.53	333.4	45	44.605
HI	316.68	314.3	49	49.444
H-HSO_4	313.86	312.5	74	72.725
TfOH	303.75	305.4	89	88.23
TosH	320.08	—	104	99.474

The first and the last terms in Eq. (1) are estimated as the difference between the sum of Gibbs free energies of the products and that of the reactants. The gas-phase Gibbs free energies are calculated by performing an analysis of the vibrational frequencies whereas the SMD implicit solvent model has been employed to compute the solvatation energies. In detail, the Integral equation formalism is implemented in polarizable continuum model (IEFPCM) by taking the electrostatic and non-electrostatic terms (cavitation, dispersion and repulsion energies) from Truhlar and coworkers' SMD solvation model[15].

To assess the accuracy of the present methodology, we calculated the enthalpy and the entropy variations $\Delta H^{\rm theo}_{298}$ and $\Delta S^{\rm theo}_{298}$ calculated using the B3LYP functional and the aug-cc-pVDZ basis set[17] for the dissociation reaction of several strong acids. The results are shown in Table 1 together with the corresponding experimental values $\Delta H^{\rm exp}_{298}$ and $\Delta S^{\rm exp}_{298}$ [17]. In both cases we observe a very good agreement between our calculations and the previous experimental and theoretical data. Finally, a second set of calculations has been carried out to establish the accuracy of the implicit solvent model described via the IEFPCM. We considered the following reaction involving pyridine in solvent water as a reference case:

$$Pyr + H^+ \rightleftharpoons PyrH^+ \quad (3)$$

The calculated value of the Gibbs free energy of reaction is $\Delta G = -8.8074$ kcal mol^{-1}, given by the sum of the three contributions of Eq. (1): in particular, $\Delta G^0 = -910.66$ kcal mol^{-1}, whereas ΔG^0 for an isolated H^+ was analytically estimated by Sackur-Tetodre formula. Importantly, the computed value of $\Delta G^{\rm theo}$ is in good agreement with the experimental one, $\Delta G^{\rm exp} = -7.0449$ kcal/mol[18].

2.2 Classical molecular dynamics

In order to investigate the effect of the proton scavenger over the morphology of PEDOT samples, we developed a novel computational tool to model the PEDOT polymerization, which allows to reproduce *in silico* the chemical processes leading from monomeric units to a polymerized sample. In the present approach molecular dynamics (MD) simulations are blended with first-principle free energy calculations (see previous section), so as to generate a fully atomistic modelling of polymerization. MD takes charge of the dynamical evolution of the system for

very long time periods whereas first-principle calculations are exploited to describe (in a probabilistic approach) the oxidative elongation processes. Specifically, the polymerization algorithm consists of two mains steps, which are iteratively repeated until the polymerized sample has been achieved: the dynamical step and the coupling step.

1. **The Dynamical step**
   The first step is responsible for the dynamical evolution of the individual EDOT monomers in the system. In all the MD runs, the positions and velocities of the interacting components are evolved according to Newton's equations of motion, as implemented in the LAMMPS molecular dynamics package[19]. The interatomic interactions are described using the AMBER force field[20], including bonding terms (bonds, angles, and dihedrals) as well as nonbonding contributions (Coulomb and van der Waals). The parameters occurring in the bonding and Van der Waals terms are taken from the GAFF database[21]. The atomic partial charges are estimated with the restrained electrostatic potential (RESP) method[22] as implemented in the Gaussian package. The velocity-Verlet algorithm with a time step of 0.5 fs is used to solve the equations of motion. A particle-particle mesh solver is used for describing the long-range electrostatic forces, and the van der Waals interaction are cut off at 0.1 nm. The Nosé-Hoover thermostat and barostat with corresponding relaxation time equal to 50 fs and 0.5 ps respectively are used.

2. **The Coupling step**
   The formation of a chemical bond between two EDOT monomers (or one EDOT monomer and one PEDOT oligomer, see Fig. 1) is accomplished in this step adopting a Markov-based approach. To this aim, we introduce a "bond creation probability" p, defined as the probability that two units can bond together forming a larger oligomer. At each time step, the distance between any pair of units is checked if smaller than a given threshold (3 Å in our case), the chemical bond is formed according to the probability p. The corresponding terms in the classical interaction potential are then eventually updated with the introduction of new bonds, angles and dihedrals. Once this step has been performed, the procedure continues with a new iteration of the dynamical step.
   In our model, we assume that different probability values p correspond to different chemical reactions according to the formula
   $$p = \min(1, \exp(\Delta G/(K_B T)) \quad (4)$$
   where K_B is the Boltzmann constant, T is the temperature and ΔG is the Gibbs free reaction energy. The bond is then formed with probability 1 if the corresponding reaction is energetically favourable ($\Delta G < 0$), otherwise it is created with a probability proportional to the Boltzmann weight.

2.3 Sample preparation

To demonstrate the capabilities of our computational tool, we emulated the polymerization process of systems as large as a cube of side 11.8 nm, containing an initial number of 10,000 EDOT monomeric units. Overall the simulation cell contained as many as 130,000 atoms. The solvent as well as the proton scavengers and tosylate molecules were not present in the simulation cell since their effect has been taken into account in the $\Delta G(n)$ calculations and therefore in the bond creation probabilities. The simulation of the polymerization process required a multi-step procedure to be performed: i) first, the monomers are placed in an initial arbitrary volume in a random fashion; ii) the system is fully relaxed at constant temperature $T = 300$ K and fixed ambient pressure using a Nosé-Hoover thermostat in order to reach the equilibrium values of volume and density; iii) the polymerization algorithm is then finally implemented keeping the temperature constant ($T = 300$ K).

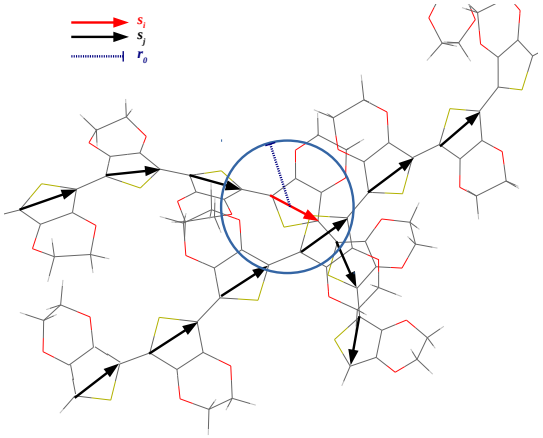

Fig. 1 Schematic representation of the orientation vectors $\vec{s}_i$ and $\vec{s}_j$ used to estimate the spatial local correlation $C(\vec{r})$

2.4 Sample crystallinity

To quantify the crystallinity of our samples, we calculated the fraction of volume v_C occupied by the crystallites. The definition of this quantity relies on the calculation of the local spatial correlation of the orientation of EDOT monomers, $C(\vec{r})$. Specifically, each EDOT unit was labeled with a vector $\vec{s}_i$ joining two carbon atoms in the thiophene ring (see Fig. 1). For each vector $\vec{s}_i$ the spatial correlation reads

$$C(\vec{r}) = \frac{1}{N} \sum_{|\vec{r}-\vec{r}_j|<r_0} |\vec{s}_i(\vec{r}) \cdot \vec{s}_j(\vec{r}_j)| \quad (5)$$

where $\vec{r}$ is the position of the first carbon atom and N is the total number of EDOT monomers. The value of r_0 was set to 5 Å . Thus, the higher is the correlation between the EDOT monomers orientations (higher values of $C(\vec{r})$), the higher is the local sample crystallinity. Therefore, by mapping the $C(\vec{r})$ values, one identifies the regions of higher crystallinity and the fraction of the sample volume occupied by crystallites v_C. $C(\vec{r})$ ranges from a minimum value of 1e-4, which characterizes samples still not polymerized, up to a maximum value of 5e-3 obtained for a perfect crystalline sample generated as reported in[13]. Four our polymerized samples, $C(\vec{r})$ ranges from 1e-4 to 9e-4. $C(\vec{r})$ is large at small distances

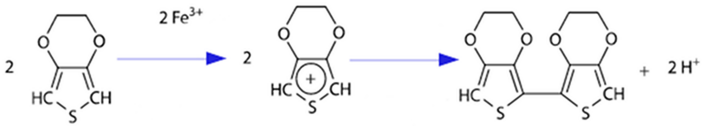

Fig. 2 Schematics of the chemical pathway for EDOT polymerization.

(where the monomer orientations are strongly correlated), but it rapidly decreases for larger distances. In the latter situation, the monomer orientations become almost uncorrelated.

From the knowledge of $C(\vec{r})$, the volume fraction occupied by crystalline regions v_C has been calculated by estimating the volume of the simulation cell for which $C(\vec{r})$ is larger than a given threshold value $C_{\min}$, i. e.:

$$v_C = \frac{\int_{C(\vec{r})>C_{\min}} dV}{V_{\text{cell}}} \tag{6}$$

We set $C_{\min} = 0.006$ at about half of the span of values taken by $C(\vec{r})$. Visual inspection of the simulation output further confirmed that the threshold set is the lowest value of C for which stacking is still observed.

3 Results

3.1 Reaction paths

Several PEDOT polymerization procedures have been reported[11], including chemical polymerization (CP), electrochemical polymerization, vapour phase polymerization (VPP) and oxidative chemical vapor deposition. In this work we will focus on the CP route, entirely occurring in solution, through an oxidative polymerization, involving five elemental reactions[3] as schematized in Fig. 2.

Neutral 3,4-ethylenedioxythiophene (EDOT) monomers are initially oxidized to form EDOT radical-cations. Many oxidizing agents have been reported, often based on

iron(III) salts (e.g.: $FeCl_3$[23] and $FeTos_3$[3]). $FeTos_3$ is currently one of the most frequently used because of its solubility in aliphatic alcohols, including buthanol and ethanol, and because of its stability[3]. In addition, $FeTos_2$ by-products do not tend to form crystalline second phases disrupting PEDOT stacking[9]. Once formed, the two radical-cations react forming a dicationic intermediate that releases two H^+, converting into a neutral dimer, with protons competitively scavenged by Brønsted bases available in the reaction environment. The dimer is then further oxidized and may react with another radical-cation to form a $(n+1)$-meric dicationic intermediate, which may then lose two protons toward a suitable base leading to the formation of a neutral $(n+1)$-mer, reentering the polymerization chain.

To identify the most effective proton scavenger for PEDOT polymerization

we considered a set of candidate chemical species and assessed their capability to bind radical-cations from a free-energy point of view. For each chemical reaction we determined via DFT the Gibbs free energy of reaction as a function of the EDOT oligomer size. Water, pyridine (Pyr) and tosylate anions (Tos^-) and every possible combination of them were considered, in a range of concentrations consistent with the experiment. Specifically, use was made of standard concentrations for the polymerization reaction as reported by Le et al.[24], namely 1 equivalent of EDOT, 2.25 equivalents of $FeTos_3$, 0.5-1.1 equivalent of pyridine.

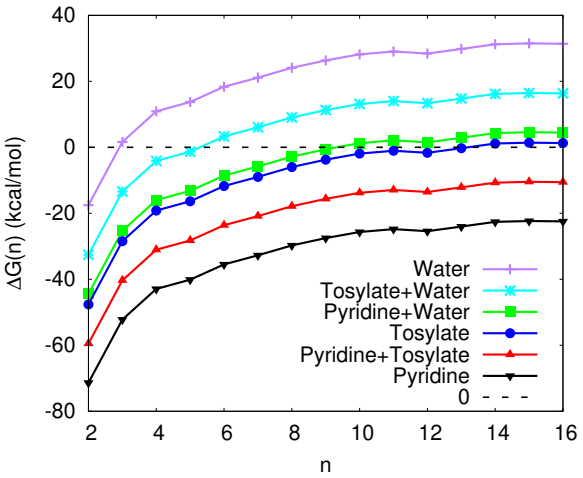

Fig. 3 Calculated Gibbs free energy $\Delta G(n)$ for the reactions 7a–7f with $2 \le n \le 16$.

The following chemical reactions were analyzed:

$$HX_{n-1}H^+ + HXH^+ + 2\,Pyr \rightleftharpoons HX_nH + 2\,PyrH^+ \tag{7a}$$

$$HX_{n-1}H^+ + HXH^+ + 2\,Tos^- \rightleftharpoons HX_nH + 2\,TosH \tag{7b}$$

$$HX_{n-1}H^+ + HXH^+ + 2\,H_2O \rightleftharpoons HX_nH + 2\,H_3O^+ \tag{7c}$$

$$HX_{n-1}H^+ + HXH^+ + Pyr + Tos^- \rightleftharpoons HX_nH + PyrH^+ + TosH \tag{7d}$$

$$HX_{n-1}H^+ + HXH^+ + Pyr + H_2O \rightleftharpoons HX_nH + PyrH^+ + H_3O^+ \tag{7e}$$

$$HX_{n-1}H^+ + HXH^+ + H_2O + Tos^- \rightleftharpoons HX_nH + H_3O^+ + TosH \tag{7f}$$

3.2 DFT evaluation of free energies of reaction

The free energies of reaction $\Delta G(n)$, computed by DFT, are shown in Fig. 3 for n ranging from 2 to 16. Since the polymerization process is spontaneous for $\Delta G(n) < 0$, the value n_c for which $\Delta G(n) = 0$ provides a first estimate of the PEDOT chain length. In the real situation, however, all reactions compete with each other since all potential scavengers are co-present.

Thermodynamic data suggest that reactions involving two pyridine molecules would dominate the process, were the stoichiometric amount of pyridine be sufficient.

This is not the case in the most common experimental scenario. If one accounts for the actual concentrations of tosylate and pyridine employed in the synthesis (1 EDOT: 7.5 Tos^-:1.1 Pyr)[24,25], one expects that pyridine will be consumed over the dimerization process. Once no pyridine is anymore available, polymerization continues with tosylate acting as proton scavenger. Therefore, the PEDOT final chain length is controlled by the tosylate, acting as

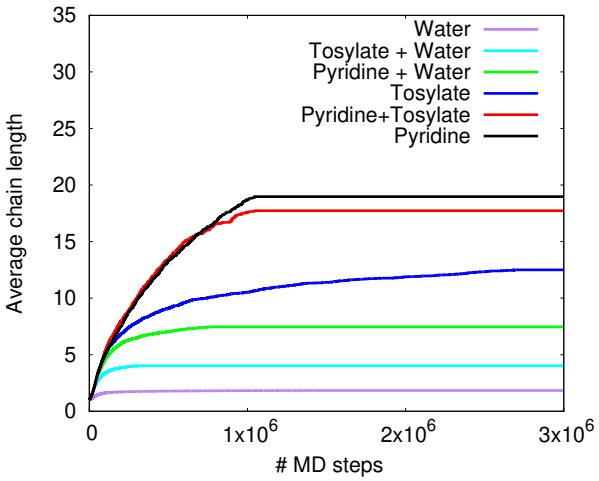

Fig. 4 Evolution of the PEDOT chain length as a function of the number of MD steps. Each of the curves corresponds to a MD simulation in which $\Delta G(n)$ values setting the bonding probability p of reactions 7a–7f are taken from Fig. 3. All the simulated polymerization reactions were run until the scavenger availability enabled the creation of new bonds.

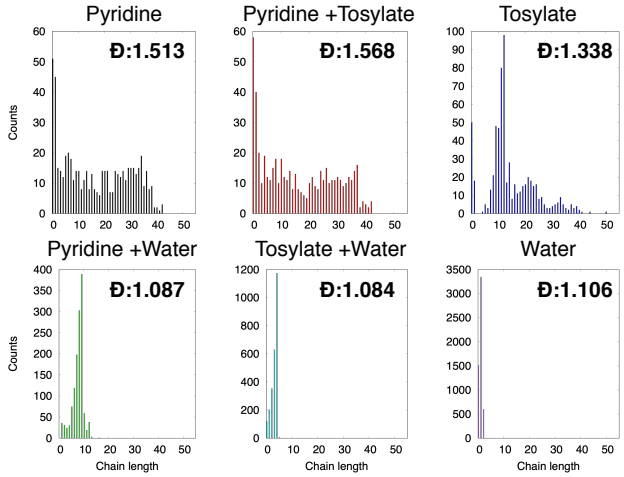

Fig. 5 Chain-length distributions and dispersity for each sample generated according to the polymerization reactions of reaction 7a–7f.

the chain-length-determining scavenger. The chain length can be preliminary estimated (blue curve in Fig. 3) to be about 12-13 monomeric units.

3.3 Classical MD calculations

To assess whether and to which extent the proton scavenger impacts the PEDOT morphology, we simulated polymerization using the MD algorithm described above. Simulations were performed for reactions 7a-7f, using DFT data of Fig. 3 to compute the reaction probabilities governing the bonding process and accounting for the specific proton scavenger. Simulations were performed on a supercell of $11.8\times11.8\times11.8$ nm^3 containing 10^4 EDOT monomers (equivalent to an initial concentration of 10.1 mol/l). The total number of steps for each MD run was $\sim3.0\times10^6$. To account for the base concentrations all simulations were run until base availability enabled the formation of new bonds. For example, in the case of pyridine, bonding was permitted up to the formation of 1.1×10^4 bonds.

The computational procedure was validated by comparing experimental and simulated X-ray diffractograms. Simulated polymerization involving tosylate as scavenger was compared to experimental data reported by Aasmundtveit *et al.*[26] concerning chemical polymerization in methanol (or butanol) solutions of $FeTos_3$ in the presence of imidazole. The experimental diffractogram shows two main peaks at 2θ =12.1° and 26.2°. The first peak was attributed to the lateral in-plane interaction between adjacent PEDOT oligomers while the second one was attributed to $\pi-\pi$ interchain stacking. The X-ray diffraction pattern computed with LAMMPS[19,27] using an incident wavelength $\lambda=1.540$ Å[28] reports a good agreement with the experiment, with the in-plane lateral and $\pi-\pi$ stacking peaks at 11.7° and 2θ =22.6°, respectively. The differences with the experimental values are expected in view of the fact that tosylate intermission between chains is not accounted for in the present simulation. Figure 4 shows the evolution of the average chain length as a function of the number of MD steps, confirming full computational convergence. As expected, the trend of the final chain lengths follows that obtained from DFT calculations (Fig. 3): pyridine gives rise to the largest chain length (∼20 monomeric units), whereas water determines the smallest one (∼4 monomeric units).

The corresponding chain length distributions are shown in Fig. 5 along with their dispersity $Đ$ (given by the ratio between the weight average molecular weight M_w and the number average molecular weight M_n)[29]. Both are strongly affected by the nature of the proton scavenger: an almost monomodal distribution is found for water with a corresponding $Đ$ of ∼1.1, whereas pyridine and tosylate yield a much broader distribution with maximum chain lengths greater than 30 and $Đ$ larger than ∼1.3.

The morphological features of PEDOT samples were further exploited by identifying (para)crystalline regions . To this aim, we computed the local spatial correlation $C(\vec{r})$ between the orientation of single EDOT units. Figure 6 shows the evolution of the sulfur-sulfur radial distribution function $g_{s-s}(r)$ (top) and of the correlation map $C(\vec{r})$ (bottom) with MD (polymerization) running time and with tosylate acting as proton scavenger. To highlight the emergence of intermolecular packing, the $g_{s-s}(r)$ has been calculated among sulphur atoms belonging to two different oligomers. The correlation maps are represented on a slab having a thickness of 1 nm. To the better identify the location of the paracrystalline regions, the PEDOT chains are plotted as black lines where each segment represents a single EDOT monomer.

The time evolution of the $C(\vec{r})$ map indicates that no crystalline regions are present in the pristine reaction ambient (0 MD steps) After 10^5 MD steps, instead, one observes the appearance of the first quasi-ordered regions. At the end of the simulation the relative volume of the crystalline regions reaches its maximum value. The analysis of the pair correlation function $g_{s-s}(r)$ indicates a clear shift towards shorter distances of all the characteristic peaks, indicating a progressive polymer packing as the crystallinity volume fraction v_C increases.

Crystallinity was further quantified through v_C (Fig. 6). A gen-

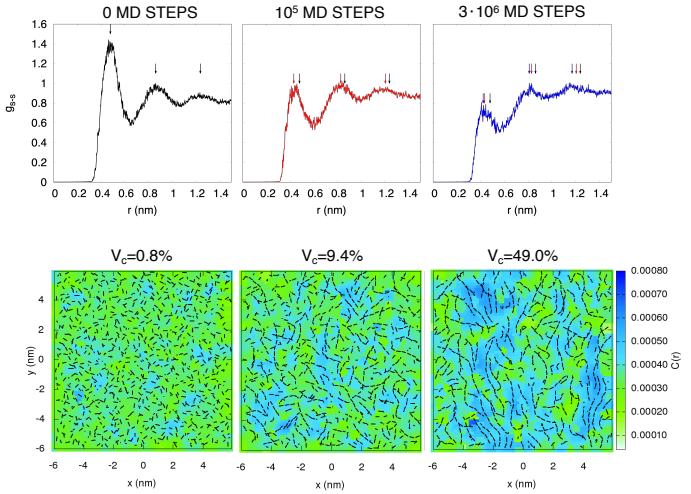

Fig. 6 Evolution of the sulfur-sulfur radial distribution function $g_{s-s}(r)$ in arbitrary units (top) and the correlation map $C(\vec{r})$ of a PEDOT sample during the simulated polymerization and with tosylate acting as proton scavenger. The correlation maps are represented on a slab having a thickness of 1 nm. The PEDOT chains are plotted as black lines, where each segment represents a single EDOT monomer. The arrows shows the position of the $g_{s-s}(r)$ peaks at 0 (black), 10^5 (red) and $3 \cdot 10^6$ MD steps (blue).

eral increase the value is observed during the polymerization, up to maximum values of 49.0 %, at the end of the simulation.

Finally, to further assess the extent to which different proton scavengers affect PEDOT morphology, we also compared the orientational correlation maps of the six samples previously generated (reactions 7a–7f).

The corresponding correlation maps (Fig. 7) show the lack of crystalline regions only with water, while for all other proton scavengers a complex network of crystalline and amorphous regions

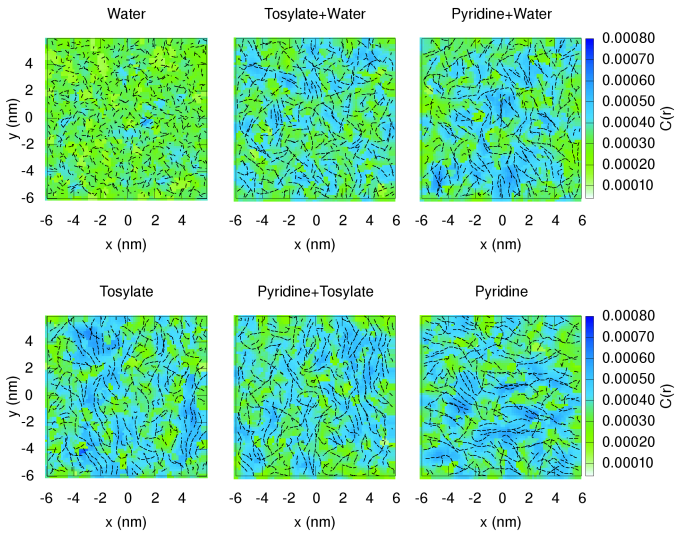

Fig. 7 Correlation maps $C(\vec{r})$ of the PEDOT samples generated according to the polymerization reactions 7a–7f.The correlation maps are represented on a slab having a thickness of 1 nm. PEDOT chains are plotted as black lines, where each segment represents a single EDOT monomer.

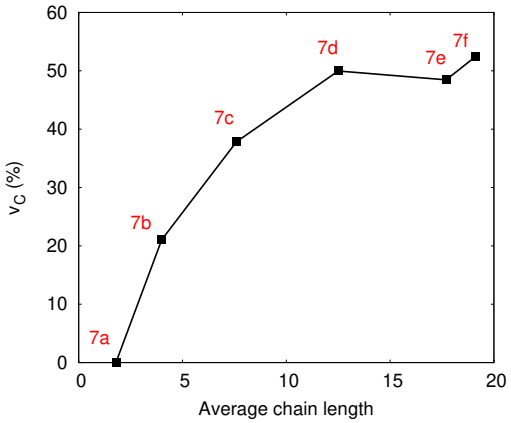

Fig. 8 Percentage of the sample volume occupied by crystallites v_C as a function of the chain length for the polymerization reactions 7a–7f .

is observed.

The corresponding values of v_C is shown in Fig. 8 as a function of the average chain length. In general, an increase of both quantities with chain length is observed. In particular, in the case of water (chain length as short as 1.8 monomeric units), v_C is as low as 0.8 %. In the opposite limit, with pyridine (average chain length of 19.1 monomeric units), the values of v_C becomes 52.4 %.

4 Discussion

Computational results confirm that crystalline regions develop during the polymerization process. To no surprise, polymerization and crystallization are concurrent processes, influencing each other during the reaction and therefore setting the final morphology. Therefore, the final structure is determined by the progressive reorganization of polymer chains while polymerization occurs.

The results in Fig. 8 show the occurrence of a complex PEDOT micromorphology in which crystalline and amorphous regions coexist. Relative volume fractions strongly depend on the average chain length. It is remarkable that with tosylate, PEDOT chain distribution is clearly multi-modal having sharper peaks than the other distributions. This *may be* consistent with speculations recently advanced[7,30] that relate PEDOT high electrical conductivity to charge percolating across amorphous regions by hopping through long polymer chains bridging separated crystalline regions. However, for these tie chains to be effective, their length should be smaller than the polymer persistence length l_p ($\sim$ 18-20 for PEDOT[12]). If such a requirement is satisfied, chains do not bend significantly, therefore retaining electronic conjugations. Based on these considerations, three main requirements are needed for percolation to enhance charge transport, namely a sufficiently high crystalline volume fraction v_C, a large fraction of chains with length smaller than l_p, and an average distance between crystalline regions comparable to l_p.

By analyzing the data of Fig. 5 and Fig. 8, tosylate emerges not only as the proton scavenger for CP but also, quite fortuitously, as the scavenger most suitable to enhance transport in PEDOT by properly setting chain length distribution. Further to

lead to a large crystalline volume fraction (v_C ∼50%) and to the largest fraction of chains with length smaller than l_p (75 %), tosylate also reports the largest amount of chains (20 %) with length comparable to the average distance between crystallites (∼ 9 monomeric units). Therefore, it may be sound to conclude that $FeTos_3$ gives rise to an utmost perfect chain length distribution, preserving a sufficiently large amount of amorphous regions to grant acceptable mechanical properties while substantially bridging crystalline, highly-conductive regions over distances for which PEDOT molecules fully retain their internal electronic conjugation.

5 Summary and Conclusions

A systematic analysis was performed to elucidate the role played by competing proton scavengers on PEDOT chain length distribution. Given the pivotal role played by the synthetic procedure in the determination of the polymer morphology, numerical simulations were carried out by concurrently enabling polymerization and structural relaxation. To this aim a novel algorithm was developed to mimic PEDOT polymerization allowing to explore how different proton scavengers affect the crystallinity fraction of the polymerized samples. It was shown how longer chains determine more crystalline samples, namely the formation of crystallites of larger dimensions. Not secondarily, we demonstrate that the formation of crystallites takes place during the polymerization, being crystallization and polymerization intrinsically concurrent processes. We also found that tosylate anions grant large crystalline fractions and an ideal combination of chain length distribution and inter-crystallite spacing for polymer charge transport.

Conflicts of interest

In accordance with our policy on Conflicts of interest please ensure that a conflicts of interest statement is included in your manuscript here. Please note that this statement is required for all submitted manuscripts. If no conflicts exist, please state that "There are no conflicts to declare".

Acknowledgements

The Acknowledgements come at the end of an article after Conflicts of interest and before the Notes and references.

Notes and references

1 Z. U. Khan, O. Bubnova, M. J. Jafari, R. Brooke, X. Liu, R. Gabrielsson, T. Ederth, D. R. Evans, J. W. Andreasen, M. Fahlman and X. Crispin, *J. Mater. Chem. C*, 2015, **3**, 10616–10623.

2 K. Wijeratne, M. Vagin, R. Brooke and X. Crispin, *J. Mater. Chem. A*, 2017, **5**, 19619–19625.

3 A. Elschner, S. Kirchmeyer, W. Lovenich, U. Merker and K. Reuter, *PEDOT: principles and applications of an intrinsically conductive polymer*, CRC Press, 2010.

4 O. Bubnova, Z. U. Khan, A. Malti, S. Braun, M. Fahlman, M. Berggren and X. Crispin, *Nature materials*, 2011, **10**, 429.

5 D. Beretta, N. Neophytou, J. M. Hodges, M. G. Kanatzidis, D. Narducci, M. Martin-Gonzalez, M. Beekman, B. Balke, G. Cerretti, W. Tremel, A. Zevalkink, A. I. Hofmann, C. Mueller, B. Doerling, M. Campoy-Quiles and M. Caironi, *Materials Science and Engineering: R: Reports*, 2018, 10.1016/j.mser.2018.09.001.

6 B. J. Worfolk, S. C. Andrews, S. Park, J. Reinspach, N. Liu, M. F. Toney, S. C. Mannsfeld and Z. Bao, *Proceedings of the National Academy of Sciences*, 2015, **112**, 14138–14143.

7 S. D. Kang and G. J. Snyder, *Nature materials*, 2017, **16**, 252.

8 A. M. Bryan, L. M. Santino, Y. Lu, S. Acharya and J. M. D'Arcy, *Chemistry of Materials*, 2016, **28**, 5989–5998.

9 F. Manrico, Z. Kamil, H. Colin and M. Peter, *Macromolecular Rapid Communications*, **29**, 1403–1409.

10 B. Winther-Jensen and K. West, *Macromolecules*, 2004, **37**, 4538–4543.

11 D. C. Martin, J. Wu, C. M. Shaw, Z. King, S. A. Spanninga, S. Richardson-Burns, J. Hendricks and J. Yang, *Polymer Reviews*, 2010, **50**, 340–384.

12 J. F. Franco-Gonzalez and I. V. Zozoulenko, *The Journal of Physical Chemistry B*, 2017, **121**, 4299–4307.

13 C. Genovese, A. Antidormi, R. Dettori, C. Caddeo, A. Mattoni, L. Colombo and C. Melis, *Journal of Physics D: Applied Physics*, 2017, **50**, 494002.

14 M. J. Frisch, G. W. Trucks, H. B. Schlegel, G. E. Scuseria, M. A. Robb, J. R. Cheeseman, G. Scalmani, V. Barone, G. A. Petersson, H. Nakatsuji, X. Li, M. Caricato, A. V. Marenich, J. Bloino, B. G. Janesko, R. Gomperts, B. Mennucci, H. P. Hratchian, J. V. Ortiz, A. F. Izmaylov, J. L. Sonnenberg, D. Williams-Young, F. Ding, F. Lipparini, F. Egidi, J. Goings, B. Peng, A. Petrone, T. Henderson, D. Ranasinghe, V. G. Zakrzewski, J. Gao, N. Rega, G. Zheng, W. Liang, M. Hada, M. Ehara, K. Toyota, R. Fukuda, J. Hasegawa, M. Ishida, T. Nakajima, Y. Honda, O. Kitao, H. Nakai, T. Vreven, K. Throssell, J. A. Montgomery, Jr., J. E. Peralta, F. Ogliaro, M. J. Bearpark, J. J. Heyd, E. N. Brothers, K. N. Kudin, V. N. Staroverov, T. A. Keith, R. Kobayashi, J. Normand, K. Raghavachari, A. P. Rendell, J. C. Burant, S. S. Iyengar, J. Tomasi, M. Cossi, J. M. Millam, M. Klene, C. Adamo, R. Cammi, J. W. Ochterski, R. L. Martin, K. Morokuma, O. Farkas, J. B. Foresman and D. J. Fox, *Gaussian∼16 Revision B.01*, 2016, Gaussian Inc. Wallingford CT.

15 A. V. Marenich, C. J. Cramer and D. G. Truhlar, *The Journal of Physical Chemistry B*, 2009, **113**, 6378–6396.

16 G. C. Shields and P. G. Seybold, *Computational approaches for the prediction of pKa values*, CRC Press, 2010.

17 K. E. Gutowski, J. D. Holbrey, R. D. Rogers and D. A. Dixon, *The Journal of Physical Chemistry B*, 2005, **109**, 23196–23208.

18 L. Sacconi, P. Paoletti and M. Ciampolini, *Journal of the American Chemical Society*, 1960, **82**, 3831–3833.

19 S. Plimpton, *Journal of computational physics*, 1995, **117**, 1–19.

20 J. W. Ponder and D. A. Case, *Advances in protein chemistry*, Elsevier, 2003, vol. 66, pp. 27–85.

21 J. Wang, R. M. Wolf, J. W. Caldwell, P. A. Kollman and D. A.

Case, *Journal of computational chemistry*, 2004, **25**, 1157–1174.

22 C. I. Bayly, P. Cieplak, W. Cornell and P. A. Kollman, *The Journal of Physical Chemistry*, 1993, **97**, 10269–10280.

23 H. Gerhard and J. Friedrich, *Advanced Materials*, **4**, 116–118.

24 T. Le Truong, N. D. Luong, J.-D. Nam, Y. Lee, H. R. Choi, J. C. Koo and H. N. Nguyen, *Macromolecular research*, 2007, **15**, 465–468.

25 D. Galliani, S. Battiston, R. Ruffo, S. Trabattoni and D. Narducci, *Journal of Physics D: Applied Physics*, 2018, **51**, 034002.

26 K. Aasmundtveit, E. Samuelsen, L. Pettersson, O. Inganäs, T. Johansson and R. Feidenhans, *Synthetic Metals*, 1999, **101**, 561–564.

27 S. Coleman, D. Spearot and L. Capolungo, *Modelling and Simulation in Materials Science and Engineering*, 2013, **21**, 055020.

28 J. F. Franco-Gonzalez and I. V. Zozoulenko, *The Journal of Physical Chemistry B*, 2017, **121**, 4299–4307.

29 M. Rogošić, H. J. Mencer and Z. Gomzi, *European polymer journal*, 1996, **32**, 1337–1344.

30 R. Noriega, J. Rivnay, K. Vandewal, F. P. Koch, N. Stingelin, P. Smith, M. F. Toney and A. Salleo, *Nature materials*, 2013, **12**, 1038.